April, 2018

2018 International Journal Remote Sensing.pdf

James E. Evans

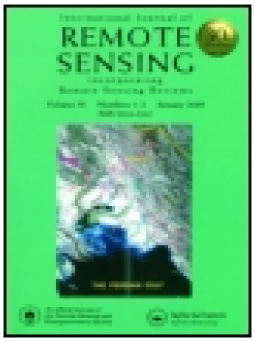

International Journal of Remote Sensing

ISSN: 0143-1161 (Print) 1366-5901 (Online) Journal homepage: http://www.tandfonline.com/loi/tres20

Multi-depth suspended sediment estimation using high-resolution remote-sensing UAV in Maumee River, Ohio

Matthew D. Larson, Anita Simic Milas, Robert K. Vincent & James E. Evans

To cite this article: Matthew D. Larson, Anita Simic Milas, Robert K. Vincent & James E. Evans (2018): Multi-depth suspended sediment estimation using high-resolution remote-sensing UAV in Maumee River, Ohio, International Journal of Remote Sensing, DOI: 10.1080/01431161.2018.1465616

To link to this article: https://doi.org/10.1080/01431161.2018.1465616

INTERNATIONAL JOURNAL OF REMOTE SENSING, 2018
https://doi.org/10.1080/01431161.2018.1465616

Taylor & Francis
Taylor & Francis Group

Multi-depth suspended sediment estimation using high-resolution remote-sensing UAV in Maumee River, Ohio

Matthew D. Larson, Anita Simic Milas, Robert K. Vincent and James E. Evans

Department of Geology, Bowling Green State University, Bowling Green, OH, USA

ABSTRACT

Satellite remote-sensing has been widely used to map suspended sediment concentration (SSC) in waterbodies. Current development of the unmanned aerial vehicle (UAV) technology allows mapping of SSC at finer spatial resolution providing high flexibility in terms of cost and acquisition time. However, the technology is immature and transfer of empirical algorithms from existing remote-sensing technologies to UAV still has to be explored. This study uses the MicaSense Sequoia sensor with four bands (green, red, red edge, and near-infrared [NIR]) mounted on-board a fixed-wing UAV to map SSC within the Maumee River in Ohio, USA, at multiple depth intervals (15, 61, 91, and 182 cm). The simple linear and stepwise regression models show the advantage of multiple bands and band ratios over single bands in mapping SSC. The findings show a limited performance of the Sequoia sensor when compared to field spectroradiometer measurements. In all cases but one, the adjusted coefficient of determination (R^2_{adj}) values is lower for the UAV data. The regression equations become similar at and below a depth of 0–61 cm, and R^2_{adj} become constant at and below a depth of 0–91 cm. While the spectroradiometer-related equations are sensitive to a wider spectral range (from green at the surface to NIR wavelength at 182 cm depth), the UAV-related equations are insensitive to green spectrum and they include a narrower spectral range (from red to NIR) over all depth increments. Field spectroradiometer measurements exhibit a strong relationship with cumulative SSC at 182 cm depth (0–182 cm) ($R^2_{\text{adj}} = 0.71$) whereas UAV reflectance data show the best relationship with SSC at 91 cm (0–91 cm) ($R^2_{\text{adj}} = 0.56$) suggesting that ~91 cm may be an optimal depth for UAV under given conditions. The results show that UAVs can be a practical but somewhat limited tool to monitor SSC in small- to medium-sized rivers.

ARTICLE HISTORY
Received 29 October 2017
Accepted 3 April 2018

1. Introduction

Suspended sediment has been an environmental concern for many decades in freshwater systems as it is one of the most common pollutants both in weight and volume (Ritchie, Zimba, and Everitt 2003; Qu 2014). Sediment can transport and store a variety of pollutants such as adsorbed phosphorus, nitrogen, pesticides, and industrial chemicals like polychlorinated biphenyls (Lodhi et al. 1998; Cousino, Becker, and Zmijewski 2015; Stow et al. 2015).

CONTACT Matthew D. Larson larsomd@bgsu.edu Department of Geology, Bowling Green State University, 190 Overman Hall, Bowling Green, OH, USA

Increased suspended sediment concentrations (SSCs) inhibit proper function of aquatic ecosystems as sediment can cause benthic smothering as well as change water chemistry (e.g. temperature, dissolved oxygen) (Lodhi et al. 1998; Branigan 2013; Qu 2014; Alighalehbabakhani et al. 2017). Additionally, high amounts of SSC can cause siltation behind dams and reservoirs limiting their efficiency as well as infill navigational channels which is economically costly (Branigan 2013; Montanher et al. 2014; Alighalehbabakhani et al. 2017).

Most of suspended sediment transport within a river happens at depth rather than at the water surface (Julien 2002). Shear stress is primarily the major mover of river sediment, which increases deeper in the water column. An increase in shear stress allows larger and more sediment particles to move downstream. The vertical SSC distribution (suspended sediment vertical profile) within a river channel is based upon the Rouse number (ratio of settling velocity to shear velocity times von Kármán's constant). Grains are settling under the influence of gravity in accord with the settling velocity (which depends on grain size, grain shape, and effective density) (Julien 2002). Grains are diffusing upward off the sediment–water interface in relationship to the applied boundary shear stress (shear velocity) through the action of turbulent eddies. If the suspended sediment vertical profile is stable, then advection of sediment downward is matched by diffusion of grains upward. Such a stable vertical profile can range from essentially zero suspended sediment transport (pure bedload transport case) if the Rouse number is a large value ($RN \gg 2.5$) to a homogeneous vertical profile (pure suspended load transport case) if the Rouse number is a small value ($RN \ll 0.8$). In general, intermediate cases would show SSCs highest at the sediment–water interface and declining logarithmically to the lowest value at the surface (Julien 2002).

In agricultural dominated watersheds, nutrient and sediment runoff are a widespread concern (Bosch et al. 2014). In Lake Erie's western basin, increased sediment load from surrounding areas and its tributaries have affected water quality in the region (Cousino, Becker, and Zmijewski 2015; Stow et al. 2015). A study done by Bosch et al. (2014) looked at how varying levels of climate change will affect sediment and nutrient runoff within western Lake Erie watersheds, as it is predicted to receive more annual precipitation and more intense springtime rain events with climate change. They found that surface sediment runoff increases on average by 13% under a moderate climate change scenario with a maximum of 39% under a more pronounced climate change scenario. The corresponding increase in surface runoff would result in increased stream SSC by 9% or 23%, respectively (Bosch et al. 2014).

Observations of spatial and temporal patterns of SSC in rivers are critical in monitoring urban, industrial, and agricultural runoff as well as predicting environmental changes that may occur due to increased SSC. Satellite remote sensing has been widely used to map SSC in larger waterbodies (e.g. oceans, lakes, estuaries, reservoirs) as field measurements are costly, time consuming, and point based (Pavelsky and Smith 2009; Montanher et al. 2014; Qu 2014; Gilvear and Bryant 2016). Studies have shown that there can be strong positive correlations between SSC and spectral reflectance within the visible and near-infrared (NIR) portion of the electromagnetic spectrum (Curran and Novo 1988; Chen, Curran, and Hansom 1992; Mertes, Smith, and Adams 1993). However, these strong correlations tend to be derived based on measurements in those large waterbodies where there is a more homogeneous mixture of suspended sediment. On the other hand, in small- to medium-sized rivers where changes of suspended sediments are temporally more dynamic and often spatially more heterogeneous, satellite remote sensing may not be always the most appropriate method. For instance, remote sensing of SSC in small rivers and streams can be limited due to coarse spatial resolution of satellite sensors (e.g. 30 m spatial resolution for Landsat 7/8; 250 m spatial resolution for MODIS). While the Very High Resolution (VHR) satellite sensors (e.g. GeoEye-1, WorldView-3, IKONOS) have the fine spatial resolution, they can be expensive to access, require planning for a new area acquisition, or only having access to data that are weeks to months old.

In recent years, the use of unmanned aerial vehicles (UAV/drone) as remote-sensing platforms has become more popular. UAVs can provide high spatial and temporal resolutions as they can be flown frequently at low altitudes (up to ~122 m), and at a desired time. They can be an essential tool to monitoring water quality in small rivers as spatial resolution can be as fine as a few centimetres (Hird et al. 2017; Zeng et al. 2017). Remote-sensing UAVs have been successfully used in various fields such as precision agriculture (Adao et al. 2017), modelling surface imperviousness for urban runoff (Tokarczyk et al. 2015), mapping river channels using lidar (Flener et al. 2013), analysing landslide dynamics (Turner, Lucieer, and de Jong 2015), as well as monitoring submerged aquatic vegetation and algae (Flynn and Chapra 2014). To our knowledge, no existing remote-sensing research addresses monitoring SSC in river channels with UAVs.

The current study is conducted in an urban and environmentally sensitive area where suspended sediment plays a critical role in the Lake Erie region. The overall goal is to assess the feasibility of using a high-resolution (13 cm) multispectral MicaSense Sequoia sensor (four bands at 530–570, 640–680, 730–740, and 770–810 nm) on-board a fixed-wing UAV to map SSC within the Maumee River. The specific objectives are to (1) explore the capabilities of a UAV to accurately estimate suspended sediments at multiple depths in small rivers and (2) evaluate which spectral bands are needed to establish an empirical relationship for mapping SSC at multi-depth intervals in the water column. Water samples are collected at 15 cm (0.5 ft), 61 cm (2 ft), 91 cm (3 ft), and 182 cm (6 ft), and cumulative SSC values (0–15, 0–61, 0–91, 0–182 cm) are correlated with the remote-sensing information. The approach depicts the cumulative SSC with depth as being observed by the sensors from above a surface water. This means that the field SSC measurements collected at a given depth must consider the SSC measurements in the water above the measured depth. The depths were chosen based on expected differences of SSC and on the depth profile of the river that ranges from 7 m in the upstream area to 6 m in the downstream area.

2. Methods

2.1. *Study site*

This study is conducted in the Western Basin of the Lake Erie region, Ohio, USA (Figure 1). The study area is a portion of the Maumee River in downtown Toledo (Figure 2(*a*)) that is approximately 1.9 km in length. The Maumee River drains the largest watershed (about 17,060 sq. km) in the Lake Erie region and enters the lake at Maumee Bay in Toledo. The Maumee River watershed's land use consists of approximately 78% agriculture, 11% urban, 7% forest, 2% wetlands, and 1% grasslands (EPA 2008). The Maumee River contributes 3% of the water flowing into Lake Erie's western basin (Moorhead, Bridgeman, and Morris 2008) but supplies about half of the sediment discharged into the lake (Cousino, Becker, and

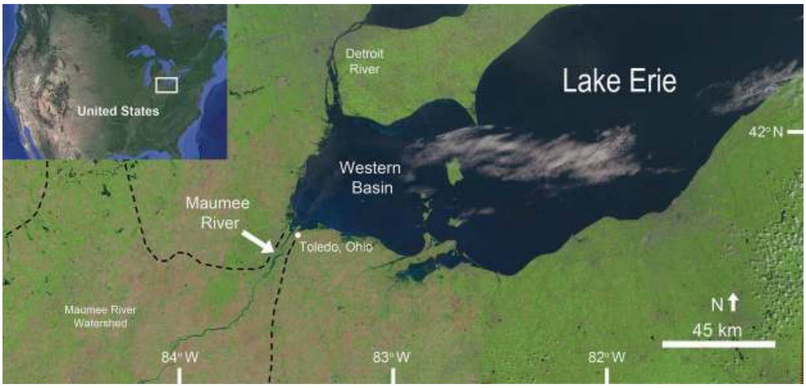

Figure 1. Location of the Western Basin of Lake Erie and Maumee River. The Maumee River Watershed is the area denoted by the dashed line.

Figure 2. (a) The area of study on the Maumee River in downtown Toledo, Ohio, USA; (b) individual water sampling locations. Location 1 is on the upstream end of the reach; location 21 is on the downstream end, closest to Maumee Bay.

Zmijewski 2015). Industrialization and agriculture in the surrounding areas have impacted the Maumee River and impaired water quality due to contaminants (Kahl et al. 2014). Much of the contaminated sediment is a result of agriculture runoff upstream (Stow et al. 2015). Suspended sediments and solids within the river are typically clay sized (or smaller) particles (Myers and Metzker 2000). The lower Maumee River has been identified by the EPA

(Environmental Protection Agency) as an Area of Concern which means it is a waterbody where beneficial uses of water resources have been significantly impacted by anthropogenic developments (USGS 2000; Cousino, Becker, and Zmijewski 2015). Deposition of sediment from the Maumee River affects the Port of Toledo and aquatic resources in the western basin of Lake Erie (Ohio Lake Erie Commission 1998). For the Maumee River, more than 870,000 m^3 of sediment is dredged every year, which costs upwards of \$2 million annually (Cousino, Becker, and Zmijewski 2015). Accurately mapping SSC on a frequent basis can help improve environmental policies as well as dredging practices.

2.2. *Field measurements*

Field measurements included water samples and surface reflectance taken on 15 October 2016 concurrently with UAV flights. Weather conditions were optimal with a temperature of 12.8°C, light winds of about 6.4 km h^{-1} out of the southwest, and high visibility.

At each sampling point (Figure 2(*b*), Table 1), a 1 l LaMotte Van Dorn water sampler was lowered to a depth of 15 cm. The sampler was left at that depth for approximately 10 s to ensure water was flowing through the sampler. The sampler was closed, brought back to the surface, and transferred into a sterile 1 l high-density polyethylene bottle. Sampler was washed with clean water between samples and process was repeated for depths of 61, 91, and 182 cm. Location, bottle number, and depth of sample were recorded. Secchi disk measurements were taken as an indicator of visual water clarity. The Secchi disk was slowly lowered down into the water column until the black and white disk disappeared from visual view and this depth was recorded.

Surface reflectance at each location was measured using a Spectral Evolution RS-3500 portable spectroradiometer approximately 100 cm above the water surface at a spatial resolution of approximately 50 cm. The spectroradiometer collects 1024 discrete measurements of reflected energy that ranges from 346.2 to 2505.4 nm (~2 nm average spectral

Table 1. Latitudes and longitudes of water sample locations.

Location	Latitude (°)	Longitude (°)
1	41.63505	−83.53234
2	41.63601	−83.53229
3	41.63768	−83.53288
4	41.63904	−83.53299
5	41.64017	−83.53337
6	41.64195	−83.53311
7	41.64391	−83.53264
8	41.64567	−83.53240
9	41.64627	−83.53200
10	41.64668	−83.53158
11	41.64765	−83.53159
12	41.64826	−83.53096
13	41.64886	−83.53046
14	41.64942	−83.53021
15	41.65066	−83.52908
16	41.65256	−83.52665
17	41.65334	−83.52526
18	41.65379	−83.52448
19	41.65407	−83.52424
20	41.65616	−83.52192
21	41.65419	−83.52323

resolution). Calibration accuracy is ±5% at 400 nm, ±4% at 700 nm, and ±7% at 2200 nm (Spectral Evolution 2017). Preprocessing of the *in situ* hyperspectral reflectance data was automatically done using the DARWin SP data acquisition software installed in the handheld data logger. The spectroradiometer also recorded locations of the field measurements (±2 m accuracy) using its own global positioning system (GPS). For this study, 404 spectral bands from the spectroradiometer between the wavelengths of 350 and 900 nm were used for analyses to compare with the UAV measurements.

2.3. *Laboratory processing*

Water samples were brought back to the laboratory for the SSC analyses (Figure 3(*a*)). SSCs were measured using USEPA Method 160.2 (Qu 2014) using GE Healthcare Whatman Grade 934-AH RTU 42.5 mm Microfiber filters. SSC was quantified by filtering a well-mixed water sample from each location (0.25 l) through a pre-dried and pre-weighed glass microfiber filter (Figure 3(*b*)). The sediment residue retained on the filters was dried in a drying oven at 103°C for 8 h, then weighed, re-dried, and weighed again for consistency (Figure 3(*c*)).

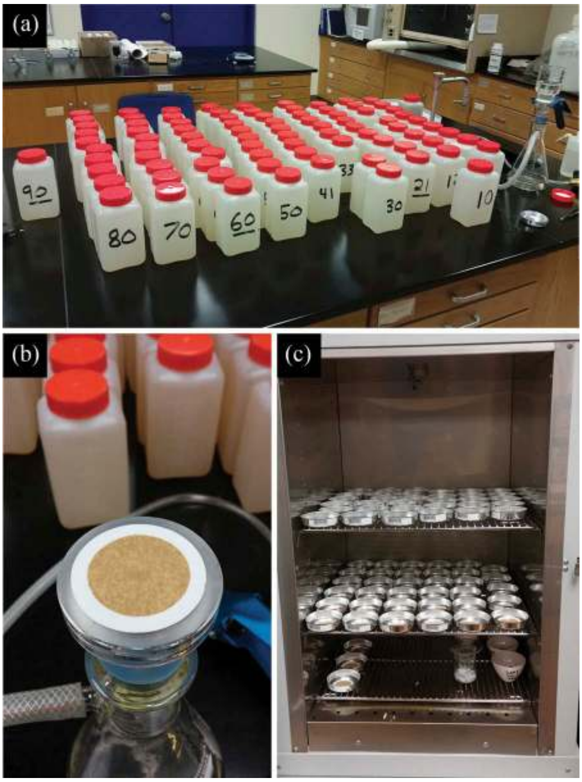

Figure 3. USEPA Method 160.2, Residue (Gravimetric) suspended solid concentration (SSC) quantification. (a) organization of river water samples being prepared for SSC filtering. (b) water sample that has just been filtered through a 42.5 mm microfiber filter. (c) filters in oven at 103°C. Each label on the filter tins represents the starting weight of that particular filter.

2.4. *UAV sensor*

The MicaSense Parrot Sequoia multispectral sensor was specifically built for the use of a drone platform. The Sequoia has four spectral bands (green, red, red edge [RE], and NIR) that have a resolution of 13 cm per pixel at 122 m above ground level and a radiometric resolution of 10 bits with a global shutter (Table 2). A sunshine sensor allows the camera to be self-calibrated. The Sequoia sensor is an independent sensor that can be mounted on fixed wing (e.g. Sensefly eBee) or multi-rotor drones (e.g. DJI Phantom series).

In this study, the MicaSense Parrot Sequoia multispectral sensor was used onboard a Sensefly eBee fixed wing drone over the study area (Figure 2(*b*)). For the first drone flight (locations 6–15), there were 728 separate images captured and for the second flight (locations 16–21), there were 212 images (Figure 2(*b*)). The limitation due to the urban setting and to the proximity of urban features to the river, several points were lost in the process of georeferencing over the water, and this caused some limitation in the number of sampling points. For instance, the drone flight over locations 1–5 did not capture enough land cover that is necessary for georeferencing of the images acquired over the river, and thus, no final images were produced over these points. Pix4D mapper software was used to stich and process the images using the drone’s GPS information and to generate reflectance measurements. The process requires some fixed targets (e.g. 20–30% land cover learned from our experience) to be able to stich and georeference the images. The flight over locations 6–15 had the most complete set of images and data points and therefore is used as a representative data set in this study.

2.5. *Statistical analyses*

Field hyperspectral (spectroradiometer) measurements were aggregated spectrally in order to simulate the bands available on the Sequoia sensor. Both aggregated field and drone reflectance data were used in the linear regression models that considered (1) single bands, (2) band ratios, and (3) combination of single bands and band ratios. Single band and band ratios were plotted against cumulative SSC with depth (0–15, 0–61, 0–91, 0–182 cm) using Origin Pro graphing software. Single bands used were green, red, RE, and NIR (Table 2). Stepwise regression models with forward selection were used in Minitab 17 to develop the relationships based on multiple bands that allowed the combination of single bands and band ratios (Vincent 2000; Pavelsky and Smith 2009; Qu 2014). The following simple band ratios were used in the analyses: green/red, green/RE, green/NIR, red/RE, red/NIR, and RE/NIR. For the regression analyses, default settings for alpha-to-enter (α_E) and alpha-to-remove (α_R) significance values were set to 0.15 ($p < 0.15$), for deciding when to enter and remove a predictor from the model.

Table 2. UAV Sequoia sensor characteristics.

Band	Spectral region	Wavelength range (nm)	Resolution (cm)
1	Green	530–570	13
2	Red	640–680	
3	RE	730–740	
4	NIR	770–810	

RE: Red edge; NIR: near-infrared.

Linear regression models were analysed at 95% (0.05) confidence interval using the adjusted coefficients of determination (R^2_{adj}) to compare results. The output of the analyses provided numerous equations with ranked R^2_{adj} values, and the highest R^2_{adj} values were used as the criteria for different water depths. R^2_{adj} was chosen over R^2 (coefficient of determination) as it considers the number of predictors in the model as well as only increases if the independent variables affect the dependent variable.

Other studies have shown that SSC and spectral response can be linear, log-linear, exponential, or logarithmic (Teodoro, Veloso-Gomes, and Goncalves 2007; Pavelsky and Smith 2009; Chen et al. 2014; Montanher et al. 2014). For the purpose of this study, linear regression models (stepwise regression model with forward selection) were chosen for model development due to its computational efficiency in selecting a model from a number of predictor variables and to reduce autocorrelation and multicollinearity (Pereira et al. 2017). Durbin–Watson statistic (d) was calculated for each regression model to test for autocorrelation and independence of variables within the model. The calculated d value is compared to upper (d_U) and lower (d_L) critical value limits based on how many variables are in the model. If d is greater than d_U, the variables are not correlated with one another. If d is less than d_L, autocorrelation exists between the variables. However, if d falls between d_L and d_U, test for autocorrelation is indeterminate.

Given the small sample sizes, the Leave-Out-One Cross-Validation (LOOCV) analysis was conducted to examine the predictive accuracy of the model (Minitab 2018). LOOCV is a specific form of cross-validation where, using an iterative approach, one data point is treated as a test set while the remaining points are considered as a training set. The analysis was done using ANOVA model between the mean square errors (MSE) of the predictive model (MSE_P) and each iteration of training data (MSE_T). The robustness of the model was examined using the test data.

3. Results

The spatial trend of SSC along the river, as observed in Figures 4(*a*)-(*d*), shows the overall increase in SSC downstream towards the mouth of the river at each depth (15, 61, 91, and 182 cm). The mean values of SSC between the sampling points vary significantly in the one-way ANOVA test ($p = 0.000$), ranging from 33.6 mg l^{-1} at a depth of 91 cm to a maximum of 68.5 mg l^{-1} at a depth of 182 cm (Table 3). The trends (rate of change and slope) generated for each depth are similar with a slightly higher variability at a depth of 91 cm. The vertical distribution of SSC, on the other hand, is relatively homogenous. The difference between the mean values is not significant in the one-way ANOVA test ($p < 0.13$) suggesting that the 182 cm water column is relatively homogenous but somewhat denser at a depth of 182 cm. The mean values of SSC at 15 and 61 cm are approximately the same at 52.2 and 52.0 mg l^{-1}, respectively. However, SSC increases with depth to 55.0 mg l^{-1} (91 cm) and to a maximum mean value of 56.3 mg l^{-1} (182 cm). All the water samples were taken within the dredge channel which had a maximum depth of 6–7 m. Visual clarity, measured by Secchi disk depth, remains relatively constant between 24 and 31 cm at all locations.

Field hyperspectral measurements exhibit a clear trend for water samples with different SSC (Figure 5). With minor exceptions, reflectance increases as SSC increases for all wavelengths. Only at wavelengths of about 375 and 875 nm, spectral profiles for SSC of 53.5 and

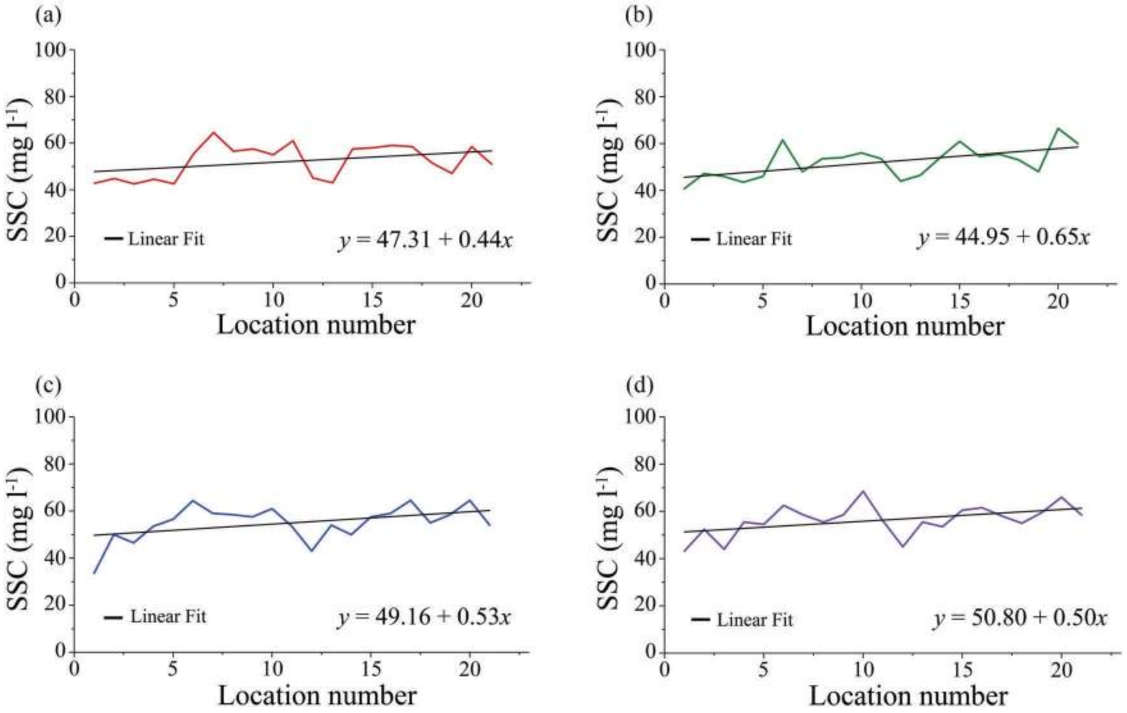

Figure 4. SSC *versus* Maumee River sampling locations. Location 1 is on the upstream end of the reach; location 21 is on the downstream end, closest to Maumee Bay. Observations at (a) 15 cm depth, (b) 61 cm depth, (c) 91 cm depth, and (d) 182 cm depth.

Table 3. Individual and cumulative SSC collected on 15 October 2016.

		Individual depth SSC (mg l^{-1})				Cumulative SSC (mg l^{-1})		
Location	Secchi disk depth (cm)	15 cm	61 cm	91 cm	182 cm	0–61 cm	0–91 cm	0–182 cm
1	31	42.8	40.8	33.6	43.2	83.6	117.2	160.4
2	27	44.8	47.2	50.0	52.4	92.0	142.0	194.4
3	24	42.5	46.0	46.5	44.0	88.5	135.0	179.0
4	31	44.5	43.5	53.5	55.5	88.0	141.5	197.0
5	27	42.5	46.0	56.5	54.5	88.5	145.0	199.5
6	31	55.5	61.5	64.4	62.5	117.0	181.4	243.9
7	31	64.5	48.0	59.0	58.5	112.5	171.5	230.0
8	27	56.5	53.5	58.5	55.5	110.0	168.5	224.0
9	24	57.5	54.0	57.5	58.5	111.5	169.0	227.5
10	27	55.0	56.0	61.0	68.5	111.0	172.0	240.5
11	31	61.0	53.5	53.5	56.0	114.5	168.0	224.0
12	31	45.0	44.0	43.0	45.0	89.0	132.0	177.0
13	31	43.0	46.5	54.0	55.5	89.5	143.5	199.0
14	24	57.5	54.0	50.0	53.5	111.5	161.5	215.0
15	31	58.0	61.0	57.5	60.5	119.0	176.5	237.0
16	31	59.0	54.5	59.0	61.5	113.5	172.5	234.0
17	27	58.5	55.5	64.5	58.0	114.0	178.5	236.5
18	31	51.5	53.0	55.0	55.0	104.5	159.5	214.5
19	24	47.0	48.0	58.5	59.5	95.0	153.5	213.0
20	27	58.5	66.5	64.5	66.0	125.0	189.5	255.5
21	31	51.0	60.0	54.0	58.5	111.0	165.5	223.5
Mean	28.5	52.2	52.0	55.0	56.3	104.2	159.2	215.5
Median	31.0	55.0	53.5	56.5	56.0	111.0	165.0	223.5
Std. dev.	2.9	7.2	6.8	7.4	6.5	12.8	18.8	24.5

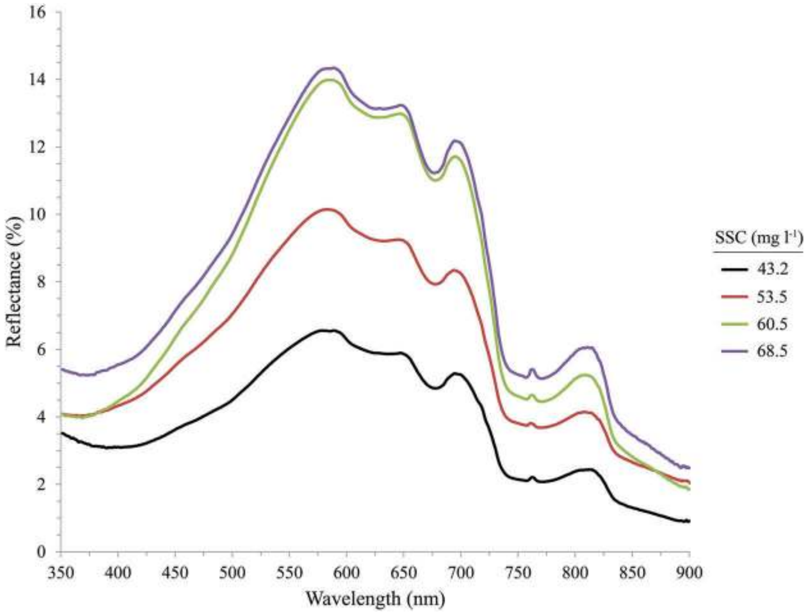

Figure 5. Reflectance profiles of water samples with various SSC collected with the field spectroradiometer.

60.5 mg l^{-1} are of the same reflectance or cross minimally. The highest reflectances are observed within the green–red spectral region with the peak at 589 nm while minimal reflectances are observed in the NIR spectral region. A steep decrease between the green–red and RE–NIR spectral regions is noticed.

Single bands in the linear regression perform poorly for both spectroradiometer and UAV measurements (equations are not included). For aggregated field hyperspectral data at different depths, the regression models yield very low R^2_{adj} values ($R^2_{\mathrm{adj}}<0.22$). Out of all single spectral bands, the highest linear R^2_{adj} is observed with the NIR spectral band ($R^2_{\mathrm{adj}} = 0.22$) at 0–182 cm depth suggesting, to a certain extent, the importance of NIR in the linear regression models at this depth. For actual Sequoia spectral bands, a cumulative SSC provides low R^2_{adj} for all single bands within the two top water depths ($R^2_{\mathrm{adj}}<0.16$). Similarly to the aggregated field hyperspectral data, the best, but still relatively low, values of R^2_{adj} are reached at deeper water increments with NIR, at both depths, 0–91 and 0–182 cm ($R^2_{\mathrm{adj}} = 0.34$) when single bands are considered.

Overall, R^2_{adj} are considerably higher for all depths when multibands are used in the stepwise regression models, with the exception of $R^2_{\mathrm{adj}} = 0.21$ at a depth of 0–91 cm for the aggregated hyperspectral data. No better R^2_{adj} was reached in the analyses for this data set and no obvious reason for this anomaly is found (Table 4). The trend of the equations involving NIR with depth is obvious in the stepwise regression analyses for both hyperspectral sensor and UAV. While NIR band is included in the equations at a depth of 0–182 cm for aggregated hyperspectral data, for the UAV data, it is already included at a depth of 0–61 cm as well as at depths of 0–91 and 0–182 cm (Tables 4 and 5). Furthermore, for field hyperspectral data, 0–15 and 0–182 cm have the best linear regression models with R^2_{adj} of 0.69 and 0.71, respectively (Table 4). No obvious trend of R^2_{adj} with water depth is observed.

For UAV Sequoia sensor data, R^2_{adj} increases from 0.32 at a depth of 0–15 cm to 0.42 at a depth of 0–61 cm and then increases to 0.56 at a depth of 0–91 cm while staying unchanged at a depth of 0–182 cm (Table 5). There is no difference between depths of 91 and 182 cm, suggesting that ~91 cm can be an optimal depth for UAV Sequoia sensors. Interestingly, the best linear models for the UAV sensor (Table 5) only consider the simple ratio that includes red–RE–NIR wavelengths. No green band and no single band factors are included in the

Table 4. Linear regression equations between SSC measurements and aggregated field spectroradiometer data.

Depth (cm)	Equation	R^2_{adj}	*d*
0–15	SSC (mg l^{-1}) = −151.2 + 384 × RE + 173.9 × (green/red)	0.69	2.59 $d_L = 0.35$ $d_U = 1.49$
0–61	SSC (mg l^{-1}) = −143.2 + 629 × RE + 202.6 × (green/red)	0.61	2.72 $d_L = 0.35$ $d_U = 1.49$
0–91	SSC (mg l^{-1}) = 235.0 − 37.8 × (red/RE)	0.21	1.98 $d_L = 0.50$ $d_U = 1.00$
0–182	SSC (mg l^{-1}) = −245 + 1369 × NIR + 372 × (green/red)	0.71	3.11 $d_L = 0.35$ $d_U = 1.49$

Spectral bands are as follows: green 530–570 nm, red 640–680 nm, red edge (RE) 730–740 nm, near-infrared (NIR) 770–810 nm.

Table 5. Linear regression equations between SSC measurements and UAV data.

Depth (cm)	Equation	R^2_{adj}	d
0–15	$\text{SSC (mg l}^{-1}) = 142.7 - 53.8 \times (\text{red/RE})$	0.32	2.16 d_L = 0.50 d_U = 1.00
0–61	$\text{SSC (mg l}^{-1}) = 226.6 - 231.9 \times (\text{red/NIR})$	0.42	2.20 d_L = 0.450 d_U = 1.00
0–91	$\text{SSC (mg l}^{-1}) = 350.1 - 365 \times (\text{red/NIR})$	0.56	2.05 d_L = 0.50 d_U = 1.003
0–182	$\text{SSC (mg l}^{-1}) = 474.2 - 495 \times (\text{red/NIR})$	0.56	2.03 d_L = 0.50 d_U = 1.00

These equations were used to make SSC maps of the Maumee River. Spectral bands are as follows: green 530–570 nm, red 640–680 nm, red edge (RE) 730–740 nm, near-infrared (NIR) 770–810 nm.

equations (Table 5). In all cases, the Durbin–Watson tests indicate that there was no autocorrelation between the variables and that they are independent of one another.

Equations presented in Table 5 were used to create SSC maps at each of the four cumulative water depth increments (Figures 6(*a*)-(*d*)). At a depth of 0–15 cm, most of the river has cumulative SSC around 30–70 mg l^{-1}. The UAV sensor captures some of the variability and increased SSC (around 90 mg l^{-1}) values along the river bank. This increased cumulative SSC is also observed and more pronounced along the bank at depths of 0–91 and 0–182 cm (Figures 6(*c*) and (*d*), respectively).

The LOOCV analysis, conducted to examine the predictive accuracy of the empirical models developed for different depths, shows no significant differences between the predictive MSE_P and MSE_T calculated for each iteration of training data (p-values = 0.488–0.830; significance level of 0.05) (Table 6). This confirms the predictive validity of the proposed models when generalized over a number of points. The smallest MSE values are observed at a depth of 0–15 cm and the errors gradually increase towards a depth of 0–182 cm, where the MSE and standard deviation (SD) of the errors become considerably higher. However, the model performs poorly over the single data points. The MSE values for the test points are highly variable and random.

4. Discussion

Using the concept of multibands and spectral ratios in empirical models based on the regression analyses is known for some time (Vincent et al. 2004; Olmanson et al. 2016; Pereira et al. 2017; Wang et al. 2017). With UAVs set to become more widely used across various fields, many existing concepts, statistical approaches, and algorithms should be validated and adjusted to UAV characteristics and capabilities to acquire spectral properties. The results in this study show an obvious advantage of using multiple bands or simple band ratios over a single band approach for UAV data. The advantage of using band ratios is to help supress the effects of atmospheric conditions and the bidirectional reflectance distribution function effects including the Sun glint on the water's surface recorded in the spectral response (Doxaran, Froidefond, and Castaing 2003; Sokoletsky et al. 2016). The impact of noise in data is reduced emphasising the spectral information of water properties.

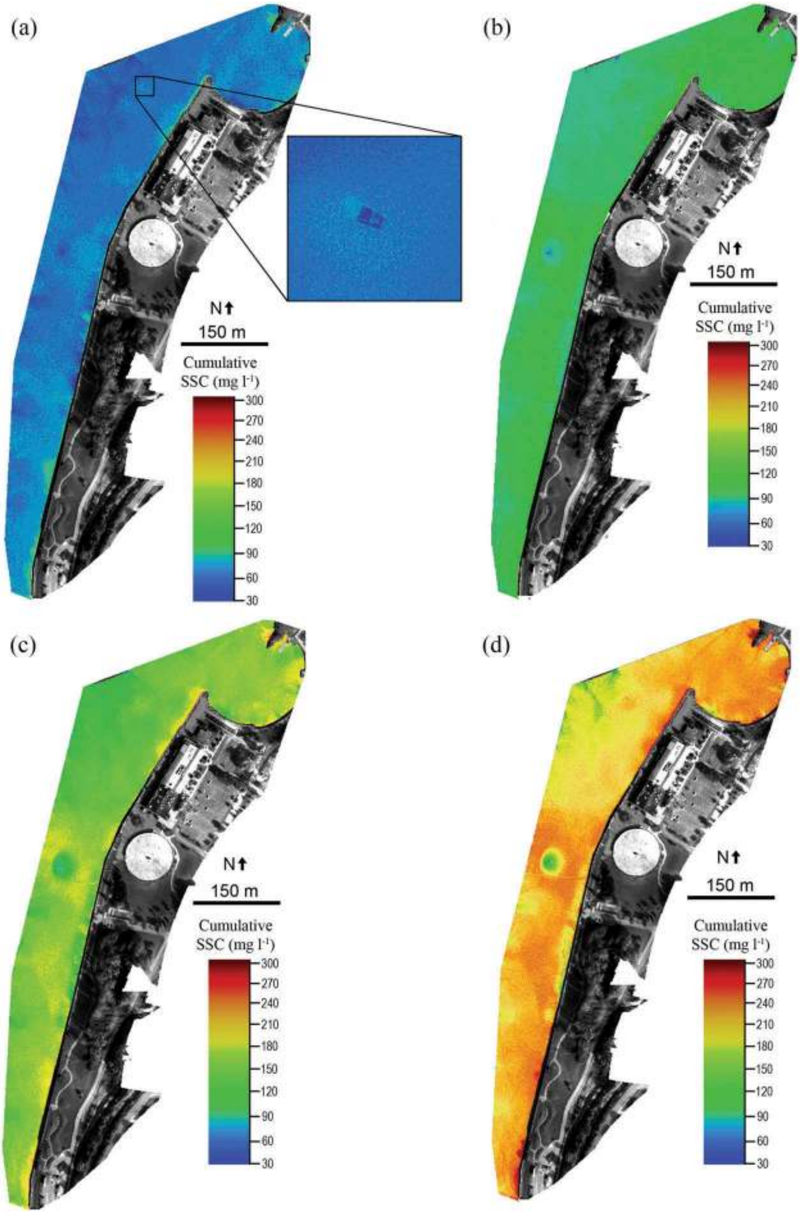

Figure 6. UAV-based cumulative SSC maps of the Maumee River in downtown Toledo. (a) Cumulative SSC from 0 to 15 cm depth. Zoomed in section is of the boat used for water sampling. Increased SSC is detected behind the boat as the propeller is mixing up the water; (b) cumulative SSC from 0 to 61 cm depth; (c) cumulative SSC from 0 to 91 cm depth; (d) cumulative SSC from 0 to 182 cm depth. Equations used for each depth are shown in Table 5.

A general shift of wavelengths from the green–red to RE–NIR spectral range with depth in the regression equations is not just obvious within each sensor but also between the sensors. While the spectroradiometer-related equations incorporate a wider range of bands (from green to NIR) and incorporate NIR at a depth of 0–182 cm, the UAV-related algorithms include

Table 6. The Leave-Out-One Cross-Validation (LOOCV) analysis: Mean Square Error of the predictive model (MSE_P) and training data (MSE_T).

	Training data		Predictive model	ANOVA MSE_P − MSE_T
Depth (cm)	MSE_T (mg l^{-1})	SD (mg l^{-1})	MSE_P (mg l^{-1})	*p*-Value
0–15	27.52	7.54	28.16	0.830
0–61	46.15	14.46	48.41	0.666
0–91	69.45	19.83	73.05	0.616
0–182	127.74	32.94	135.27	0.488

SD represents standard deviation of MSE_T. *p*-Value is based on the ANOVA analysis between MSE_P and MSE_T.

a narrower band range (from red to NIR), resembling equations at a depth of 0–61 cm and below, and having constant R^2_{adj} below a depth of 0–91 cm. While the spectroradiometer has a better potential of capturing SSC at deeper depths, the resembling equations and constant R^2_{adj} beyond the depth of 0–61 cm suggest that the UAV sensor has limited capabilities of capturing SSC with depth. Although no algae was observed in the water during the field campaign, the green band included in the spectroradiometer-related equations may suggest some presence of algae in the near-surface water layer that was not captured by the UAV sensor.

There is a progressive increase in spectral reflectance with an increase of SSC (Lodhi et al. 1998; Shen et al. 2010). For clear water, it is expected that the red–RE–NIR wavelengths become more absorbed and thus less reflective with depth than green wavelength. On the other hand, for turbulent water, higher SSC exhibits higher reflectance in all optical wavelengths, especially in the red and NIR wavelengths of the spectrum (Doxaran et al. 2002; Sokoletsky et al. 2016). With the cumulative increase of SSC from the surface to a depth of 182 cm, the progressive increase of SSC is observed, from 104.2 to 215.5 mg l^{-1} (Table 3), and it is the increase of SSC that most likely causes the wavelength shift towards RE and NIR with depth. Also, somewhat higher than usual (in October), SSC contributes to a general trend of increasing reflectance in all wavelengths. Even though the weather on this particular day was clear with light winds, it was likely that the relatively high SSC, when compared with our previous field measurements in the summer (mean: 46–49 mg l^{-1} [18 May 2016], 11.5–16.8 mg l^{-1} [3 June 2016], 20.8–22.7 mg l^{-1} [19 June 2016]), was due to time of year (Bosch et al. 2014; Eder et al. 2014). Land use of areas upstream of sampling locations is predominantly used for agriculture. Crops are commonly harvested in early October, and exposed soil is more susceptible to sediment runoff during this period (Bosch et al. 2014).

The indications of limiting capabilities of the UAV sensor to capture SSC at a deeper depth could be due to several reasons such as the impact of the atmosphere and glint effect, coarser spectral resolution, as well as too small spatial resolution (13 cm) when compared with the spectroradiometer (50 cm). It is surmised that 13 cm is not an optimal spatial resolution to capture SSC at deeper depths given that the georeferencing process of UAV data is still a research challenge. The roughness of the water can produce glitter, which can backscatter more light into the sensor increasing the noise in an image.

The field SSC measurements suggest insignificant difference between measured mean SSC within the water column (Table 3), and almost identical spatial trends of SSC at each depth along the river (Figure 4). The water column is essentially homogenous (known as pure suspended load transport conditions) although the values are increasing slightly from a water surface towards a depth of 182 cm. In reality, remote-sensing data should match cumulative SSC values with increasing depth, because the response at a depth of 182 cm is the combined effect of the response at depths of 15, 61, 91, and 182 cm.

The local SSC variations could commonly occur due to the transient effects of turbulent eddies which are bringing high suspended sediment water upwards and low SSCs downwards (Julien 2002). Eddies are commonly generated near flow boundaries (e.g. near the channel bed) and surfacing near the shore can be expected due to friction with shore features (e.g. rocks or submerged logs) (Yalin 1992; Julien 2002). This may be the reason for the low R^2_{adj} ($R^2_{\text{adj}} = 0.21$) observed for the spectroradiometer-related equations derived for a depth of 0–91 cm.

General trend of SSC increases towards the mouth of the river downstream has been expected as more sediment is accumulating at the mouth before being deposited in Maumee Bay. In the UAV suspended sediment maps, extremely high SSC was detected along the eastern edge of the river at depths of 15, 91, and 182 cm. A plausible cause of the increased SSC at the bottom of Figure 6 is due to the sediments influent that comes from the nearby construction site where the new International Park Storage Basin project started prior to the data collection (Toledo Waterways Initiative 2017). A way to visually examine the accuracy of the SSC map is by observing the water sampling boat, present at each map (as enlarged in Figure 6(*a*)) as well as the increase in SSC likely due to interaction between the propeller and water. When the propeller is engaged, it effectively mixes the upper portion of the water column and can cause increased local SSC for a finite period of time.

Some uncertainties should be recognized in this study. Loss of some points due to low land coverage in the images has limited this study to a certain extent. Some further improvements such as more precise georeferencing, which represents an ongoing challenge concerning UAVs data acquisition, are needed. Although the aggregation of hyperspectral bands may affect the selection of bands used in the algorithms, it does not have a major impact on the results. While water samples and field hyperspectral measurements were taken at the same time of UAV flights, the actual image acquisition and the collection of field hyperspectral measurements were several minutes apart. This may cause some uncertainties in the results as water surface roughness may change on a matter of seconds at a given location. The blue band was not available in this study; however, it is not expected that this band would provide better results, as it is commonly not critical to the SSC detection. The results in this study are derived based on a 1 day field campaign and further data collection should be done in future studies to help verify the results.

Overall, the study presents a pioneering effort to contribute to understanding how new low cost high spatial and temporal resolution sensors can monitor SSC in small/medium-sized rivers. The Sequoia sensor is widely available and assessable to researchers; thus, helping to understand its performance over water is critical to future studies.

5. Conclusion

This study explored the capabilities of the MicaSense Parrot Sequoia multispectral sensor onboard a Sensefly eBee UAV of capturing SSC in the Maumee River at multiple depth intervals (15, 61, 91, and 182 cm). The field hyperspectral spectroradiometer was used to collect field reflectance measurements and water samples were collected to measure SSCs using USEPA Method 160.2. The simple linear and stepwise regression models showed the advantage of multiple bands and band ratios over single bands used in the models for both spectroradiometer and UAV sensor. The results suggested somewhat limited performance of the Sequoia sensor when compared to the spectroradiometer. Generally, the R^2_{adj} values were lower for the UAV data; the regression equations become similar at and below a depth of 0–61 cm, and R^2_{adj} become constant below a depth of 0–91 cm suggesting that ~91 cm may be an optimal depth for UAV under given conditions. A general shift of wavelengths with depth was observed in the modelling equations within each sensor and between the sensors. While the spectroradiometer-related equations were sensitive to a wider spectral range (from green at the surface to NIR at a depth of 0–182 cm), the UAV-related equations were insensitive to the green band and they included a narrower spectral range (from red to NIR) over all depth increments. The indications of limiting capabilities of the UAV sensor could be due to several reasons such as the impact of the atmosphere and glint effect, coarser spectral resolution, as well as too small spatial resolution, which may be related to imprecision in georeferencing of the UAV images.

Disclosure statement

No potential conflict of interest was reported by the authors.

ORCID

Matthew D. Larson http://orcid.org/0000-0002-4148-8618

References

Adao, T., J. Hruska, L. Padua, J. Bessa, E. Peres, R. Morais, and J. J. Sousa. 2017. “Hyperspectral Imaging: A Review on UAV-Based Sensors, Data Processing and Applications for Agriculture and Forestry.” *Remote Sensing* 9: 1110. doi:10.3390/rs9111110.

Alighalehbabakhani, F., C. J. Miller, J. P. Selegean, J. Barkach, S. M. S. A. Abkenar, T. Dahl, and M. Baskaran. 2017. “Estimates of Sediment Trapping Rates for Two Reservoirs in the Lake Erie Watershed: Past and Present Scenarios.” *Journal of Hydrology* 544: 147–155. doi:10.1016/j.jhydrol.2016.11.032.

Bosch, N. S., M. A. Evans, D. Scavia, and J. D. Allan. 2014. “Interacting Effects of Climate Change and Agricultural BMPs on Nutrient Runoff Entering Lake Erie.” *Journal of Great Lakes Research* 40: 581–589. doi:10.1016/j.jglr.2014.04.011.

Branigan, J. 2013. “Development of a Field Test for Total Suspended Solids Analysis.” PhD diss., University of Nebraska Lincoln.

Chen, J., T. Cui, Z. Qiu, and C. Lin. 2014. “A Three-Band Semi-Analytical Model for Deriving Total Suspended Sediment Concentration from HJ-1A/CCD Data in Turbid Coastal Waters.” *ISPRS Journal of Photogrammetry and Remote Sensing* 93: 1–13. doi:10.1016/j.isprsjprs.2014.02.011.

Chen, Z., P. J. Curran, and J. D. Hansom. 1992. “Derivative Reflectance Spectroscopy to Estimate Suspended Sediment Concentration.” *Remote Sensing of Environment* 40: 7–77. doi:10.1016/0034-4257(92)90127-6.

Cousino, L. K., R. H. Becker, and K. A. Zmijewski. 2015. “Modeling the Effects of Climate Change on Water, Sediment, and Nutrient Yields from the Maumee River Watershed.” *Journal of Hydrology: Regional Studies* 4: 762–775. doi:10.1016/j.ejrh.2015.06.017.

Curran, P. J., and E. M. M. Novo. 1988. “The Relationship between Suspended Sediment Concentration and Remotely Sensed Spectral Radiance: A Review.” *Journal of Coastal Research* 4 (3): 351–368.

Doxaran, D., J. M. Froidefond, and P. Castaing. 2003. "Remote-Sensing Reflectance of Turbid Sediment-Dominated Waters. Reduction of Sediment Type Variations and Changing Illumination Conditions Effects by Use of Reflectance Ratios." *Applied Optics* 42 (15): 2623–2634. doi:10.1364/AO.42.002623.

Doxaran, D., J. M. Froidefond, S. Lavender, and P. Castaing. 2002. "Spectral Signature of Highly Turbid Waters. Application with SPOT Data to Quantify Suspended Particulate Matter Concentrations." *Remote Sensing of Environment* 81: 149–161. doi:10.1016/S0034-4257(01)00341-8.

Eder, A., M. Exner-Kittridge, P. Strauss, and G. Bloschl. 2014. "Re-Suspension of Bed Sediment in Small Stream – Results from Two Flushing Experiments." *Hydrology and Earth System Sciences* 18: 1043–1052. doi:10.5194/hess-18-1043-2014.

EPA. 2008. "Evaluation of Land Use/Land Cover Characteristics in Ohio Drainages to Lake Erie." *Ohio Phosphorus Task Force*, October 1. Accessed 20 January 2018. http://www.epa.ohio.gov/portals/35/lakeerie/ptaskforce/OPTF_Landuse_20081001_hres.pdf

Flener, C., M. Vaaja, A. Jaakkola, A. Krooks, H. Kaartinen, A. Kukko, E. Kasvi, H. Hyyppa, J. Hyyppa, and P. Alho. 2013. "Seamless Mapping of River Channels at High Resolution Using Mobile LiDAR and UAV-Photography." *Remote Sensing* 5: 6382–6407. doi:10.3390/rs5126382.

Flynn, K. F., and S. C. Chapra. 2014. "Remote Sensing of Submerged Aquatic Vegetation in a Shallow Non-Turbid River Using an Unmanned Aerial Vehicle." *Remote Sensing* 6 (12): 12815–12836. doi:10.3390/rs61212815.

Gilvear, D., and R. Bryant. 2016. "Analysis of Remotely Sensed Data for Fluvial Geomorphology and River Science." In *Tools in Fluvial Geomorphology,* edited by G. Mathias Kondolf and Herve Piegay. Chichester, UK: John Wiley & Sons.

Hird, J. N., A. Montaghi, G. J. McDermid, J. Kariyeva, B. J. Moorman, S. E. Nielsen, and A. C. S. McIntosh. 2017. "Use of Unmanned Aerial Vehicles for Monitoring Recovery of Forest Vegetation on Petroleum Well Sites." *Remote Sensing* 9 (5): 413. doi:10.3390/rs9050413.

Julien, P. Y. 2002. *River Mechanics*. Cambridge: Cambridge University Press.

Kahl, M. D., D. L. Vileneuve, K. Stevens, A. Schroeder, and E. A. Makynen. 2014. "An Inexpensive, Temporally Integrated System for Monitoring Occurrence and Biological Effects of Aquatic Contaminants in the Field." *U.S. Environmental Protection Agency Papers*, 237. http://digitalcommons.unl.edu/usepapapers/237

Lodhi, M. A., D. C. Rundquist, L. Han, and M. S. Kuzila. 1998. "Estimation of Suspended Sediment Concentration in Water Using Integrated Surface Reflectance." *Geocarto International* 13 (2): 11–15. doi:10.1080/10106049809354637.

Mertes, L. A. K., M. O. Smith, and J. B. Adams. 1993. "Estimating Suspended Sediment Concentrations in Surface Waters of the Amazon River Wetlands from Landsat Images." *Remote Sensing of Environment* 43: 281–301. doi:10.1016/0034-4257(93)90071-5.

Minitab. 2018. "Model Summary Table for Fit Regression Model." Accessed 12 March 2018. https://support.minitab.com/en-us/minitab/18/help-and-how-to/modeling-statistics/regression/how-to/fit-regression-model/interpret-the-results/all-statistics-and-graphs/model-summary-table/#r-sq-pred

Montanher, O. C., E. M. L. M. Novo, C. C. F. Barbosa, C. D. Renno, and T. S. F. Silva. 2014. "Empirical Models for Estimating the Suspended Sediment Concentration in Amazonian White Water Rivers Using Landsat 5/TM." *International Journal of Applied Earth Observation and Geoinformation* 29: 67–77. doi:10.1016/j.jag.2014.01.001.

Moorhead, D., T. Bridgeman, and J. Morris. 2008. "Changes in Water Quality of Maumee Bay 1928-2003." *Checking the Pulse of Lake Erie* 123–158. www.jstor.org/stable/10.14321/j.ctt1bmzpdx.10.

Myers, D. N., and K. D. Metzker. 2000, "Status and Trends in Suspended-Sediment Discharges, Soil Erosion, and Conservation Tillage in the Maumee River Basin-Ohio, Michigan, and Indiana." *USGS Water-Resources Investigations Report 00-409*. Accessed 31 January 2018. https://oh.water.usgs.gov/reports/wrir/wrir00-4091.pdf

Ohio Lake Erie Commission. 1998. *State of the Lake Report, Lake Erie Quality Index*, 88. Toledo, Ohio: Ohio Lake Erie Commission.

Olmanson, L. G., P. L. Brezonik, J. C. Finlay, and M. E. Bauer. 2016. "Comparison of Landsat 8 and Landsat 7 for Regional Measurements of CDOM and Water Quality in Lakes." *Remote Sensing of Environment* 185: 119–128. doi:10.1016/j.rse.2016.01.007.

Pavelsky, T. M., and L. C. Smith. 2009. “Remote Sensing of Suspended Sediment Concentration, Flow Velocity, and Lake Recharge in the Peace-Athabasca Delta, Canada.” *Water Resources Research* 45: 11. doi:10.1029/2008WR007424.

Pereira, L. S. F., L. C. Andes, A. L. Cox, and A. Ghulam. 2017. “Measuring Suspended-Sediment Concentrations and Turbidity in the Middle Mississippi and Lower Missouri Rivers Using Landsat Data.” *Journal of the American Water Resources Association (JAWRA)* 1–11. doi:10.1111/1752-1688.12616.

Qu, L. 2014. “Remote Sensing Suspended Sediment Concentration in the Yellow River.” PhD diss., University of Connecticut.

Ritchie, J. C., P. V. Zimba, and J. H. Everitt. 2003. “Remote Sensing Techniques to Assess Water Quality.” *Photogrammetric Engineering & Remote Sensing* 69 (6): 695–704. doi:10.14358/PERS.69.6.695.

Shen, F., M. S. Salama, Y. Zhou, J. Li, Z. Su, and D. Kuang. 2010. “Remote-Sensing Reflectance Characteristics of Highly Turbid Estuarine Waters – A Comparative Experiment of the Yangtze River and the Yellow River.” *International Journal of Remote Sensing* 31 (10): 2639–2654. doi:10.1080/01431160903085610.

Sokoletsky, L., S. Fang, X. Yang, and X. Wei. 2016. “Evaluation of Empirical and Semianalytical Spectral Reflectance Models for Surface Suspended Sediment Concentration in the Highly Variable Estuarine and Coastal Waters of East China.” *IEEE Journal of Selected Topic in Applied Earth Observations and Remote Sensing* 9 (11): 5182–5192. doi:10.1109/JSTARS.2016.2582909.

Spectral Evolution. 2017. “RS-3500 Remote Sensing Portable Spectroradiometer Bundle.” Accessed 29 October 2017. www.spectralevolution.com/portable_spectroradiometer_RS-3500.html

Stow, C. A., Y. Cha, L. T. Johnson, R. Confesor, and R. P. Richards. 2015. “Long-Term and Seasonal Trend Decomposition of Maumee River Nutrient Inputs to Western Lake Erie.” *Environmental Science and Technology* 49: 3392–3400. doi:10.1021/es5062648.

Teodoro, A. C., F. Veloso-Gomes, and H. Goncalves. 2007. “Retrieving TSM Concentration from Multispectral Satellite Data by Multiple Regression and Artificial Neural Networks.” *IEEE Transactions on Geoscience and Remote Sensing* 45 (5): 1342–1350. doi:10.1109/TGRS.2007.893566.

Tokarczyk, P., J. P. Leitao, J. Rieckermann, K. Schindler, and F. Blumensaat. 2015. “High-Quality Observation of Surface Imperviousness for Urban Runoff Modelling Using UAV Imagery.” *Hydrology and Earth System Sciences* 19: 4215–4228. doi:10.5194/hess-19-4215-2015.

Toledo Waterways Initiative. 2017. *International Park Storage Basin*, April 24. Accessed 30 October 2017. http://www.toledowaterwaysinitiative.com/media/4-24-17-CPAC-International-Park-Basin-Presentation.pdf

Turner, D., A. Lucieer, and S. M. de Jong. 2015. “Time Series Analysis of Landslide Dynamics Using an Unmanned Aerial Vehicle (UAV).” *Remote Sensing* 7 (2): 1736–1757. doi:10.3390/rs70201736.

USGS. 2000. “Status and Trends in Suspended-Sediment Discharges, Soil Erosion, and Conservation Tillage in the Maumee River Basin-Ohio, Michigan, and Indiana: Water Resources Investigations.” Report 00-4091.

Vincent, R. K. 2000. “Forecasts of Monthly Averaged Daily Temperature Highs in Bowling Green, Ohio from Monthly Sea Surface Temperature Anomalies in the Eastern Pacific Ocean during the Previous Year.” *Photogrammetric Engineering & Remote Sensing* 66 (8): 1001–1009.

Vincent, R. K., X. Qin, R. M. L. McKay, J. Miner, K. Czajkowski, J. Savino, and T. Bridgeman. 2004. “Phycocyanin Detection from LANDSAT TM Data for Mapping Cyanobacterial Blooms in Lake Erie.” *Remote Sensing of Environment* 89: 381–392. doi:10.1016/j.rse.2003.10.014.

Wang, Z., K. Kawamura, Y. Sakuno, X. Fan, Z. Gong, and J. Lim. 2017. “Retrieval of Chlorophyll-A and Total Suspended Solids Using Iterative Stepwise Elimination Partial Least Squares (ISE-PLS) Regression Based on Field Hyperspectral Measurements in Irrigation Ponds in Higashihiroshima, Japan.” *Remote Sensing* 9: 264. doi:10.3390/rs9030264.

Yalin, M. S. 1992. *River Mechanics*. New York: Pergamon Press.

Zeng, C., D. J. King, M. Richardson, and B. Shan. 2017. “Fusion of Multispectral Imagery and Spectrometer Data in UAV Remote Sensing.” *Remote Sensing* 9 (7): 696. doi:10.3390/rs9070696.